Dynamic Analysis of Wind Turbine Planetary Gears Using an Extended Harmonic Balance Approach

Preprint

Y. Guo and J. Keller
National Renewable Energy Laboratory

R. Parker
The Ohio State University

To be presented at International Conference on Noise and Vibration Engineering
Leuven, Belgium
September 17-19, 2012

NREL is a national laboratory of the U.S. Department of Energy, Office of Energy Efficiency & Renewable Energy, operated by the Alliance for Sustainable Energy, LLC.

Conference Paper
NREL/CP-5000-55355
June 2012

Contract No. DE-AC36-08GO28308

Available electronically at http://www.osti.gov/bridge

Available for a processing fee to U.S. Department of Energy
and its contractors, in paper, from:

U.S. Department of Energy
Office of Scientific and Technical Information
P.O. Box 62
Oak Ridge, TN 37831-0062
phone: 865.576.8401
fax: 865.576.5728
email: mailto:reports@adonis.osti.gov

Available for sale to the public, in paper, from:

U.S. Department of Commerce
National Technical Information Service
5285 Port Royal Road
Springfield, VA 22161
phone: 800.553.6847
fax: 703.605.6900
email: orders@ntis.fedworld.gov
online ordering: http://www.ntis.gov/help/ordermethods.aspx

Cover Photos: (left to right) PIX 16416, PIX 17423, PIX 16560, PIX 17613, PIX 17436, PIX 17721

Printed on paper containing at least 50% wastepaper, including 10% post consumer waste.

Dynamic Analysis of Wind Turbine Planetary Gears Using an Extended Harmonic Balance Approach

Yi Guo[1], **Jonathan Keller**[1], **Robert G. Parker**[2]
[1] National Renewable Energy Laboratory
15013 Denver West Parkway, Golden, CO 80401-3305 USA
email: **yi.guo@nrel.gov**

[2] The Ohio State University, USA
University of Michigan-Shanghai Jiao Tong University Joint Institute, China

Abstract

The dynamics of wind turbine planetary gears with gravity effects are investigated using an extended harmonic balance method that includes simultaneous internal and external excitations. This method along with arc-length continuation and Floquet theory is applied to a lumped-parameter planetary gear model including gravity, fluctuating mesh stiffness, bearing clearance, and nonlinear tooth contact to obtain the planetary gear dynamic response. The calculated responses compare well with time-domain-integrated mathematical models and experimental results. Gravity is a fundamental vibration source in wind turbine planetary gears and plays an important role in system dynamics, causing hardening effects induced by tooth wedging and bearing-raceway contacts. Bearing clearance significantly reduces the lowest resonant frequencies of translational modes. Gravity and bearing clearance together lower the speed at which tooth wedging occurs below the resonant frequency.

Nomenclature

b	Backlash
$\mathbf{f}$, $\mathbf{F}$	Force vector
i	Harmonic number
I	Inertia
k	Support stiffness
L	Characteristic length
M	Characteristic mass
N	Number of planets
m,n,p,q	Sidebands
r	Base radius
R	Number of harmonics
u	Rotational displacement
x, y	Translations of the carrier, ring, and sun
$\mathbf{x}$, $\mathbf{z}$	System degrees of freedom
β	Helix angle
Δ	Bearing clearance
η, ξ	Translations of the planets *wrt* carrier
θ	Rotational displacement
τ	Time
ω	Characteristic frequency
Ω_1, Ω_2	Excitation frequencies
ψ	Pressure angle

Subscripts

B	Bearing
c	Carrier
m	Mesh
p	Planet
r	Ring
s	Sun
$1, 2 \ldots N$	Planet number

Superscripts

b	Back-side
d	Drive-side

1 Introduction

Planetary gears have been used in wind turbines for decades because of their compact design and high efficiency. The majority of wind turbines use a horizontal axis configuration; thus, gravity becomes a periodic excitation source in the rotating carrier frame. Prior study of gravity by the authors was performed with a static analysis and focused on the effect of gravity upon bearing force and tooth wedging in a spur wind turbine planetary gear [1]. It was found that tooth wedging, an abnormal contact situation where the tooth is in contact with both drive-side and back-side flanks simultaneously, can be caused by gravity. Tooth wedging increases planet-bearing forces and disturbs load sharing among the planets, which could lead to premature bearing failure.

Nonlinear dynamics induced by bearing clearance has been studied for relatively small-geared systems. Kahraman and Singh [2] observed chaos in the dynamic response of a geared rotor-bearing system with bearing clearance and backlash. Gurkan and Ozguven [3] studied the effects of backlash and bearing clearance in a geared flexible rotor and the interactions between these two nonlinearities. Guo and Parker [4] investigated the nonlinear effects and instability caused by bearing clearance in helicopter planetary gears. Dynamic effects of bearing clearance in wind turbine planetary gears have not been studied in the past because the wind turbine operating speed was believed to be well below the frequency range of drivetrain dynamics. However, bearing clearance reduces some gearbox resonances significantly.

The finite element program developed by Vijayakar [5] uses a combined surface integral and finite element approach to capture tooth deformation and contact loads in geared systems. This finite element model includes bearing clearance, tooth separation, tooth wedging, fluctuating mesh stiffness, and gravity. Numerical integration is widely adopted to compute dynamic responses of mechanical systems in the time domain. Ambarisha and Parker [6] employed numerical integration to study nonlinear dynamics and the impacts of mesh phasing on vibration reduction of planetary gears. Velex and Flamand [7] used numerical integration results of a planetary gear with time-varying mesh stiffness as a benchmark to evaluate results from a Ritz method.

The harmonic balance method [8] is a nonlinear, frequency-domain, steady-state simulation for mechanical systems. Zhu and Parker [9] used this method to study clutch engagement loss in a belt-pulley system. Blankenship and Kahraman [10] studied the dynamics of a mechanical oscillator with clearance nonlinearity and fluctuating mesh stiffness, and correlated results with experimental data [11]. Al-shyyab and Kahraman [12][13] investigated primary resonances, subharmonic resonances, and chaos in a multimesh gear train caused by fluctuating gear mesh stiffness. Bahk and Parker [14] employed harmonic balance to analyze planetary gear dynamics based on a purely rotational model. Use of the harmonic balance method reduces computational time for lightly damped or physically unstable systems with long transients by avoiding the long transient decay time before a steady state is reached. Compared to numerical integration and finite element analysis that are widely adopted approaches to compute dynamic responses, the computation time of the harmonic balance method is one to two orders of magnitude lower. Harmonic balance often employs arc-length continuation [15] and Floquet theory [16][17] to calculate nonlinear resonances in the dynamic response, including unstable solutions that numerical integration and finite element analysis are unable to obtain. The established harmonic balance formulation is only suitable for systems with one fundamental excitation frequency and its higher harmonics. However, wind turbine drivetrains have simultaneous internal and external excitations, including fluctuating mesh stiffness, gravity, bending-moment-induced excitations in the rotating carrier frame, wind shear, tower shadow, and other aero-induced excitations.

This study develops a modified harmonic balance method to obtain the dynamic response of wind turbine planetary gears including excitations from gravity, excitations from fluctuating mesh stiffness, and nonlinearities from bearing clearance. The coupling effects between these two excitations are considered by including their side bands. Other excitation sources can be considered in a similar way. The proposed method is validated by comparing calculated results against available experimental data and other established computational approaches.

2 Lumped-Parameter Model for Planetary Gears

A previously developed lumped-parameter model whose results were correlated with finite element analyses was adopted for this paper [1][4]. As depicted in Figure 1(a), the carrier, ring, sun, and planets are rigid bodies, each having two translational and one rotational degree of freedom. The two-dimensional model has $3(N + 3)$ degrees of freedom. The model includes bearing clearance, tooth wedging, tooth separation, fluctuating mesh stiffness, and gravity. Bearings are modeled using circumferentially distributed radial springs with a uniform clearance. This study focuses on the nonlinear carrier bearing with clearance as shown in Figure 1(b). Planet-bearing clearance is not included because its dynamic effects on low-speed resonances are negligible [4].

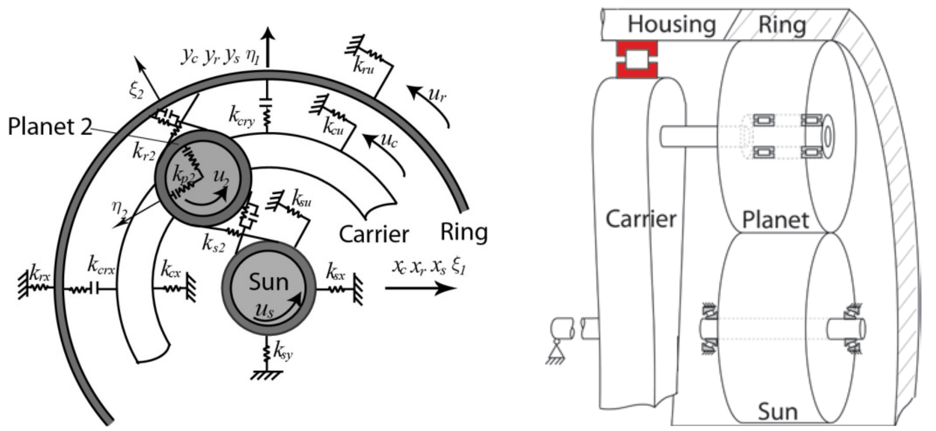

(a) (b)

Figure 1: (a) The planetary gear lumped-parameter model [1] and (b) side view of the planetary gear

The equations of motion of planetary gears are nondimensionalized as

$$\tilde{\mathbf{M}}\mathbf{z}'' + \tilde{\mathbf{C}}\mathbf{z}' + \tilde{\mathbf{f}}_m^d(\tau,\mathbf{z}) + \tilde{\mathbf{f}}_m^b(\tau,\mathbf{z}) + \tilde{\mathbf{f}}_B(\tau,\mathbf{z}) = \tilde{\mathbf{F}}(\tau)$$
$$\mathbf{z} = \frac{\mathbf{x}}{L},\ \tilde{\mathbf{M}} = \frac{\mathbf{M}}{M},\ \tilde{\mathbf{C}} = \frac{\mathbf{C}}{ML\omega},\ \tilde{\mathbf{f}}_m^d = \frac{\mathbf{f}_m^d}{ML\omega^2},\ \tilde{\mathbf{f}}_m^b = \frac{\mathbf{f}_m^b}{ML\omega^2},\ \tilde{\mathbf{f}}_B = \frac{\mathbf{f}_B}{ML\omega^2},\ \tilde{\mathbf{F}} = \frac{\mathbf{F}}{ML\omega^2} \tag{1}$$

Derivations of **M**, **C**, **f**, and **F** are detailed in [1]. Excitations used in the model include gravity-induced excitation in the rotating carrier frame and fluctuating mesh stiffness. Gravitational force acting on the carrier, ring, sun, and planets is periodic in the rotating carrier frame, resulting in a fundamental external excitation source. The mesh stiffness fluctuates as the number of teeth in contact changes and is also an important internal excitation source of geared systems. These excitations are included through time-varying mesh stiffnesses.

2.1 Extended harmonic balance method with arc-length continuation

The extended harmonic balance method is developed to obtain dynamic responses of the model in Eq. (1). The formulation includes two excitation sources with excitation frequencies Ω_1 and Ω_2. The response **z** is expanded into a Fourier series and assumed to include the R_1, R_2, $R_3R_4R_5$, and $R_6R_7R_8$ harmonics of excitation frequencies Ω_1 and Ω_2 and their side bands $m\Omega_1 + n\Omega_2$ and $p\Omega_1 - q\Omega_2$. Each component z_h in **z** then has a total of $2(R_1 + R_2 + R_3R_4R_5 + R_6R_7R_8) + 1$ terms and is expressed as:

$$
\begin{aligned}
z_h &= \bar{z}_{h,1} + \sum_{i=1}^{R_1}\left[\bar{z}_{h,2i}\cos i\Omega_1\tau + \bar{z}_{h,2i+1}\sin i\Omega_1\tau\right] + \sum_{i=1}^{R_2}\left[\bar{z}_{h,2(i+L_1)}\cos j\Omega_2\tau + \bar{z}_{h,2(i+L_1)+1}\sin i\Omega_2\tau\right] \\
&+\sum_{i=1}^{R_5}\sum_{m=1}^{R_4}\sum_{n=1}^{R_3}\left\{\bar{z}_{h,2[n+L_2+(m-1)R_3+(i-1)R_3R_4]}\cos i(m\Omega_1+n\Omega_2)\tau + \bar{z}_{h,2[n+L_2+(m-1)R_3+(i-1)R_3R_4+1]}\sin i(m\Omega_1+n\Omega_2)\tau\right\} \\
&+\sum_{i=1}^{R_8}\sum_{p=1}^{R_7}\sum_{q=1}^{R_6}\left\{\bar{z}_{h,2[q+L_3+(p-1)R_6+(i-1)R_6R_7]}\cos i(p\Omega_1-q\Omega_2)\tau + \bar{z}_{h,2[q+L_3+(p-1)R_6+(i-1)R_6R_7+1]}\sin i(p\Omega_1-q\Omega_2)\tau\right\}
\end{aligned}
\quad (2)
$$

where

$L_1 = R_1$, $L_2 = R_1 + R_2$

and $L_3 = R_1 + R_2 + R_3R_4R_5$

The response vector transforms into $\mathbf{z} = \mathbf{\Gamma}\bar{\mathbf{z}}$ by defining a function $\mathbf{\Gamma}$ that maps the response from the Fourier domain to the time domain.

$$
\mathbf{\Gamma} = \begin{pmatrix} \ddots & & \\ & \mathbf{\Gamma}_1 + \mathbf{\Gamma}_2 + \sum_m\sum_n \mathbf{\Gamma}_3(m,n) + \sum_p\sum_q \mathbf{\Gamma}_4(p,q) & \\ & & \ddots \end{pmatrix} \quad (3)
$$

The functions $\mathbf{\Gamma}_1$, $\mathbf{\Gamma}_2$, $\mathbf{\Gamma}_3$, and $\mathbf{\Gamma}_4$ are defined in [18]. The Fourier coefficient vector $\bar{\mathbf{z}}$ is defined as:

$$
\bar{\mathbf{z}} = \begin{bmatrix} \underbrace{\bar{z}_{1,1},\cdots,\bar{z}_{1,2L_1+1}}_{x_c(\Omega_1)},\underbrace{\cdots,\bar{z}_{1,2L_2+1}}_{x_c(\Omega_2)},\underbrace{\cdots,\bar{z}_{1,2L_3+1},\cdots,\bar{z}_{1,L_4}}_{x_c(\Omega_1,\Omega_2)},\cdots, \\ \underbrace{\bar{z}_{3N+3,1},\cdots,\bar{z}_{3N+3,2L_1+1}}_{u_N(\Omega_1)},\underbrace{\cdots,\bar{z}_{3N+3,2L_2+1}}_{u_N(\Omega_2)},\underbrace{\cdots,\bar{z}_{3N+3,2L_3+1},\cdots,\bar{z}_{3N+3,L_4}}_{u_N(\Omega_1,\Omega_2)} \end{bmatrix}^T \quad (4)
$$

where $L_4 = 2\left(R_1 + R_2 + R_3R_4R_5 + R_6R_7R_8\right) + 1$.

The response derivatives are then transformed into

$$
\begin{aligned}
\mathbf{z}'' &= -\mathbf{\Gamma}\Omega_1^2\mathbf{A_1}\bar{\mathbf{z}} - \mathbf{\Gamma}\Omega_2^2\mathbf{A_2}\bar{\mathbf{z}} - \mathbf{\Gamma}\sum_m\sum_n(m\Omega_1+n\Omega_2)^2\mathbf{A_3}\bar{\mathbf{z}} - \mathbf{\Gamma}\sum_p\sum_q(p\Omega_1-q\Omega_2)^2\mathbf{A_4}\bar{\mathbf{z}} \\
\mathbf{z}' &= \mathbf{\Gamma}\Omega_1\mathbf{B_1}\bar{\mathbf{z}} + \mathbf{\Gamma}\Omega_2\mathbf{B_2}\bar{\mathbf{z}} + \mathbf{\Gamma}\sum_m\sum_n(m\Omega_1+n\Omega_2)\mathbf{B_3}\bar{\mathbf{z}} + \mathbf{\Gamma}\sum_p\sum_q(p\Omega_1-q\Omega_2)\mathbf{B_4}\bar{\mathbf{z}}
\end{aligned}
\quad (5)
$$

where the operators **A** and **B** are also defined in [18]. The nonlinear force vectors, detailed in [4][18], are transformed as:

$$
\tilde{\mathbf{f}}_m^d = \mathbf{\Gamma}\bar{\mathbf{f}}_m^d, \tilde{\mathbf{f}}_m^b = \mathbf{\Gamma}\bar{\mathbf{f}}_m^b, \tilde{\mathbf{f}}_B = \mathbf{\Gamma}\bar{\mathbf{f}}_B, \tilde{\mathbf{F}} = \mathbf{\Gamma}\bar{\mathbf{F}} \quad (6)
$$

Substituting Eq. (5) and Eq. (6) into the equations of motion Eq. (1) yields

$$
\begin{aligned}
&\mathbf{\Gamma}\{[-\Omega_1^2\mathbf{MA_1} - \Omega_2^2\mathbf{MA_2} - \sum_m\sum_n(m\Omega_1+n\Omega_2)^2\mathbf{MA_3} - \sum_p\sum_q(p\Omega_1-q\Omega_2)^2\mathbf{MA_4} + \\
&\qquad \Omega_1\mathbf{B_1} + \Omega_2\mathbf{B_2} + \sum_m\sum_n(m\Omega_1+n\Omega_2)\mathbf{CB_3} + \sum_p\sum_q(p\Omega_1-q\Omega_2)\mathbf{CB_4} \\
&\qquad\qquad + \mathbf{K}_{LTI}]\bar{\mathbf{z}} + (\bar{\mathbf{f}}_B + \bar{\mathbf{f}}_m^d + \bar{\mathbf{f}}_m^b) - \bar{\mathbf{F}}\} = 0
\end{aligned}
\quad (7)
$$

where $\mathbf{K}_{LTI}$ is the time-invariant stiffness matrix. The function $\mathbf{\Gamma}$ is not singular, so it can be eliminated from both sides of Eq. (7). By defining

$$\bar{\mathbf{K}} = -\Omega_1^2\mathbf{MA_1} - \Omega_2^2\mathbf{MA_2} - \sum_m\sum_n (m\Omega_1 + n\Omega_2)^2\mathbf{MA_3} - \sum_p\sum_q (p\Omega_1 - q\Omega_2)^2\mathbf{MA_4} + \\ \Omega_1\mathbf{B_1} + \Omega_2\mathbf{B_1} + \sum_m\sum_n (m\Omega_1 + n\Omega_2)\mathbf{CB_3} + \sum_p\sum_q (p\Omega_1 - q\Omega_2)\mathbf{CB_4} + \mathbf{K}_{LTI} \tag{8}$$

Eq. (7). then becomes

$$\bar{\mathbf{K}}\bar{\mathbf{z}} = \bar{\mathbf{F}} - \bar{\mathbf{f}}_B - \bar{\mathbf{f}}_m^d - \bar{\mathbf{f}}_m^b \tag{9}$$

By using these derivations, the ordinary differential equations of motion in Eq. (1) are transformed into the linear equations in Eq. (7). The computational effort required to solve Eq. (7) compared to Eq. (1) is significantly less. The Global Newton method can be used to calculate solutions of Eq. (7). The Jacobian matrix **J** for the Global Newton iteration is defined as

$$\mathbf{J} = \frac{\partial(\bar{\mathbf{K}}\bar{\mathbf{z}} - \bar{\mathbf{f}}_B - \bar{\mathbf{f}}_m^d - \bar{\mathbf{f}}_m^b)}{\partial\bar{\mathbf{z}}} \tag{10}$$

Smoothing functions are employed to approximate the piecewise nonlinear forces so that the exact formulation of **J** can be derived. These nonlinear forces include bearing reaction forces and tooth loads on the drive-side and back-sides of the gears [4]. The inverse Fourier transformation operator **H** is defined such that $\bar{\mathbf{z}} = \mathbf{Hz}$, which maps from the time domain to the frequency domain.

$$\mathbf{H} = \begin{pmatrix} \ddots & & \\ & \mathbf{H}_1 + \mathbf{H}_2 + \sum_m\sum_n \mathbf{H}_3(m,n) + \sum_p\sum_q \mathbf{H}_4(p,q) & \\ & & \ddots \end{pmatrix} \tag{11}$$

The explicit formation of **J** is obtained as

$$\mathbf{J} = \mathbf{K}_{LTI} + \mathbf{H}\frac{\partial\mathbf{f}_B}{\partial\bar{\mathbf{z}}}\mathbf{L} + \mathbf{H}\frac{\partial\mathbf{f}_m^d}{\partial\bar{\mathbf{z}}}\mathbf{L} + \mathbf{H}\frac{\partial f_m^b}{\partial\bar{\mathbf{z}}}\mathbf{L} \tag{12}$$

J can be approximated numerically by employing finite difference algorithms [19]. The numerical determination of **J** is time consuming in high dimensional space. Furthermore, its accuracy depends on the step size of the finite difference algorithms and can be disrupted by computational round-off errors. The solution for $\bar{\mathbf{z}}$ after ν iterations is given by

$$\bar{\mathbf{z}}^{\nu+1} = \bar{\mathbf{z}}^{\nu} + \left[\mathbf{J}^{\nu}\left(\bar{\mathbf{z}}^{\nu}\right)\right]^{-1} \cdot \mathbf{f}^{\nu}\left(\bar{\mathbf{z}}^{\nu}\right) \tag{13}$$

where

$\mathbf{f}^{\nu}(\bar{\mathbf{z}}^{\nu})$ is the residue of Eq. (9) after ν iterations.

Using the line search technique [20] for the Newton method improves the iteration convergence rate [4]. Arc-length continuation traces coexisting stable and unstable solutions of the dynamic response. The initial guess is determined by choosing the direction of the next solution to be perpendicular to the direction of the previous solution as shown in Figure 2. The iteration convergence rate relies on the initial guess and the step size in the arc-length direction. If the solution curve is rather flat, the step size is selected to be large. If the current solution is near resonances, the step size is reduced to capture the turning points [4].

$$\begin{pmatrix} J(\bar{\mathbf{z}}^{\nu};\alpha^{\nu}) & \dfrac{\partial f(\bar{\mathbf{z}}^{\nu};\Omega^{\nu})}{\partial\Omega} \\ (\bar{\mathbf{z}}^{\nu} - \bar{\bar{\mathbf{z}}})^T & \Omega^{\nu} - \bar{\Omega} \end{pmatrix} \begin{pmatrix} d\bar{\mathbf{z}}^{\nu} \\ d\Omega^{\nu} \end{pmatrix} = \begin{pmatrix} -f(\bar{\mathbf{z}}^{\nu};\Omega^{\nu}) \\ 0 \end{pmatrix} \tag{14}$$

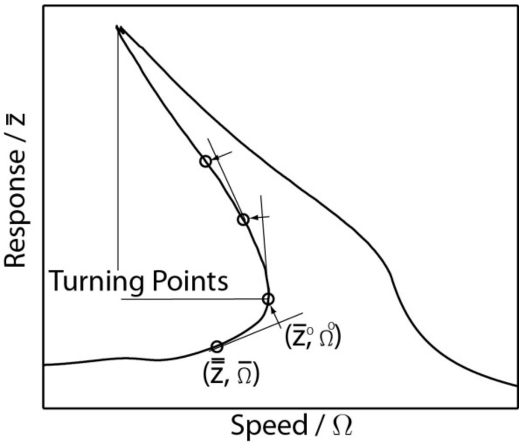

Figure 2: Successive iterations using arc-length continuation scheme

3 Gearbox Description

This study investigates a 750-kW wind turbine planetary gear (PG-A) used by the National Renewable Energy Laboratory (NREL) Gearbox Reliability Collaborative (GRC) [21] and a 550-kW wind turbine planetary gear (PG-B) [1, 22]. These two gearboxes have similar configurations and are representative of the majority of three-point mounted wind turbine drivetrains. Experiments on PG-A provide a benchmark for the lumped-parameter model using the extended harmonic balance method; however, the relevant available experimental data for PG-A is only at a single speed. Results from the extended harmonic balance method are also compared to the time integrated results of the lumped-parameter model of PG-B within the speed range of 0 to 200 Hz.

PG-A is configured in a helical planetary gear arrangement with two parallel stages. The three-point mounted drivetrain has a main bearing that supports the rotor and input shaft and two trunnion mounts that support the gearbox. Within the gearbox, there are two cylindrical roller bearings supporting the carrier, each with 275 μm of clearance. The planetary gear is arranged in an in-phase bridged carrier design with three equally spaced planets. The sun pinion shaft is connected to the intermediate stage through a spline joint that partially floats the sun pinion. The ring gear is bolted to the gearbox housing. The rated torque is 322,610 Nm and the rated speed of the input shaft is 22.2 rpm [23]. PG-B is configured in a spur planetary gear arrangement with two parallel stages. Like PG-A, PG-B has three equally spaced planets. The rated torque is 180,000 Nm and the rated speed is 30 rpm [1, 22]. Additional key parameters of these two gearboxes are listed in the Appendix. A large ring gear mass in these designs results from a typical wind turbine gearbox arrangement whereby much of the gearbox housing is rigidly connected to the ring.

4 Model Comparisons

4.1 Comparison to experimental data

The dynamic response of PG-A is computed using the extended harmonic balance method at rated speed and rated torque. Five percent modal damping is assumed for PG-A based on the modal damping extracted from a numerical torque impulse test of the PG-B finite element model. Torque applied to the lumped-parameter model is scaled to exclude the out-of-plane tooth loads caused by the planet gear helix angle. The translational displacement of the carrier over a carrier cycle computed using the extended harmonic balance method is compared against the experimental data measured in the GRC project [21] as shown in Figure 3. The agreement between the extended harmonic balance method and experimental data is reasonably good in capturing the maximum displacement amplitude.

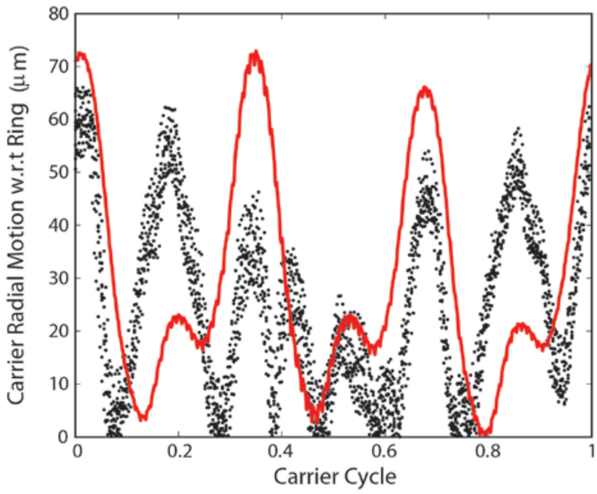

Figure 3: Carrier radial displacement with respect to the ring calculated using the extended harmonic balance method (-) and measured by the GRC project (…)

The frequency spectrum of the carrier displacement is shown in Figure 4. A modal component at 6P (six times the carrier rotational frequency) is dominant in the frequency spectrum of the measured signal. The passing frequency of the carrier pin bores could be the main contributor to this 6P component. The carrier is a bridged design and thus has three pin bores on both the upwind and downwind sides. These two circular sets of pin bores are misaligned because of manufacturing tolerances and torque windup in operation, which could be the cause of the 6P excitation. This 6P component might also be caused by the in-plane deformation of the carrier rim due to its varying thickness [24]. The magnitude of the 6P component is 25% of the 1P magnitude for the calculated carrier displacement. The lumped-parameter model considers the carrier as a single lumped mass; thus, it does not consider the detailed carrier geometry. Consequently, the lumped parameter method underestimates the magnitude of the displacement at 6P. In addition, the displacement amplitude of the first mesh frequency harmonic at 99P is more than an order of magnitude lower than the displacements at the low-speed excitations (1P–6P) for both the calculated and measured results.

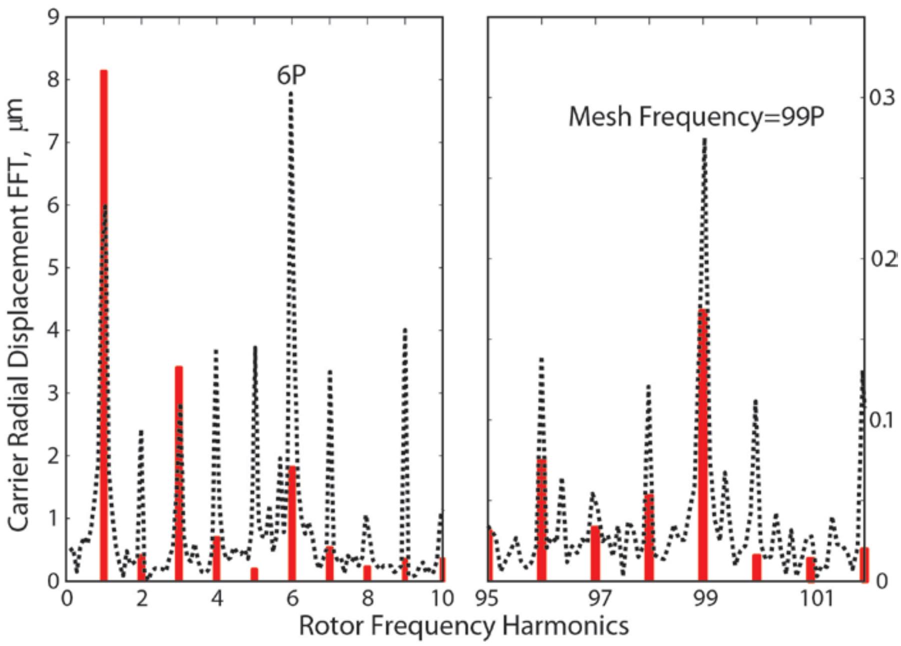

Figure 4: Frequency spectrum of the measured (…) and calculated (-) carrier displacement

Calculated planet-bearing forces are compared against the experimental data in Figure 5. The mean and fluctuating amplitudes of bearing forces computed by the extended harmonic balance method largely match those of the experimental data. The planet-bearing force for each individual planet bearing over a carrier cycle is asymmetric because of different pin position errors and bearing clearances for each planet. The lumped-parameter model predicts a 1.4% difference between the peak amplitudes of the planet-bearing forces over a carrier cycle because of these errors and clearances. The measured bearing force of planet 2 deviates from the other two planets, which suggests that planet 2 could have been mislocated or the experimental data for planet 2 could include an offset in error. The measured signal on planet 2 is currently under investigation for accuracy.

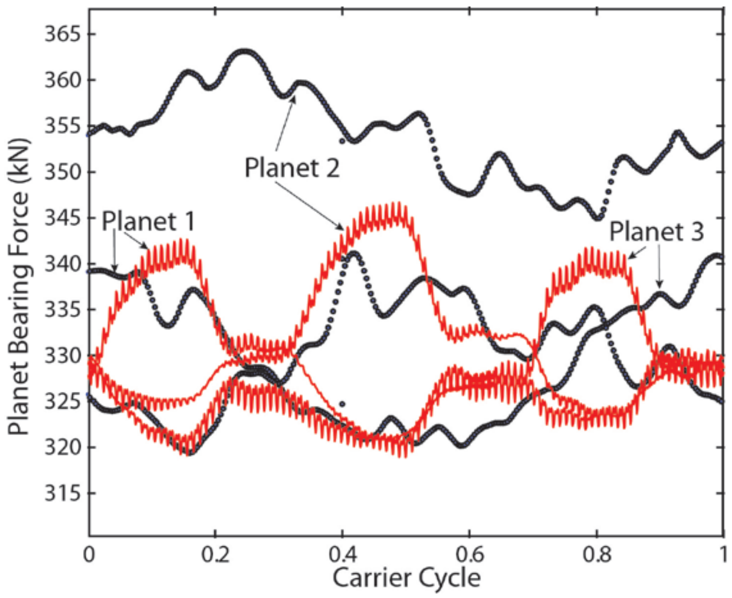

Figure 5: Measured (…) and calculated (-) planet-bearing forces over a carrier cycle

4.2 Comparison to numerical integration

Dynamic response results computed by the extended harmonic balance method are compared against finite element and numerical integration analyses for PG-B. In lightly damped systems, finite element analysis and numerical integration require many time steps for the transient response to diminish so that steady-state data can be obtained. The extended harmonic balance method avoids these long duration integration simulations by calculating the steady-state dynamic response in the frequency domain.

The numerical integration methods include results for increasing and decreasing speeds. The steady-state response at the prior speed is the initial guess for the succeeding speed. Numerical integration and finite element analysis compute only stable responses. Conversely, the harmonic balance method uses arc-length continuation to find unstable responses by tracing solutions as the speed changes quasi-statically.

The natural frequencies of PG-B below 400 Hz without bearing clearance and nonlinear tooth contact are listed in Table 3 in the Appendix. Modal analysis is performed numerically on the finite element model of PG-B by applying torque and force impulses at the carrier and sun. Numerical impulse tests provide natural frequencies and their mode shapes as described in Table 3. The natural frequencies predicted by the lumped-parameter model match those obtained by the finite element approach. The modal damping ratios are extracted from the frequency response functions obtained from numerical impulse tests of the finite element model, with damping ratios obtained from the half-power points of the resonances listed in Table 3.

Quasi-static results of the lumped-parameter model have been correlated with finite element analyses [1]. Translational displacements of the ring and sun are compared for the extended harmonic balance and numerical integration methods in Figure 6. The agreement between these two methods is very good up to 100 Hz. The nonlinear resonance at 40 Hz is due to the stiffening effect of tooth wedging. Using speed sweeps, numerical integration predicts nonlinear jumps in the dynamic response. Harmonic balance calculates the unstable branches between these nonlinear jumps, denoted by the symbol (○) in Figure 6. The agreement among the proposed method, numerical integration, and finite element analysis validates this method for predicting nonlinear dynamic responses of wind turbine planetary gears.

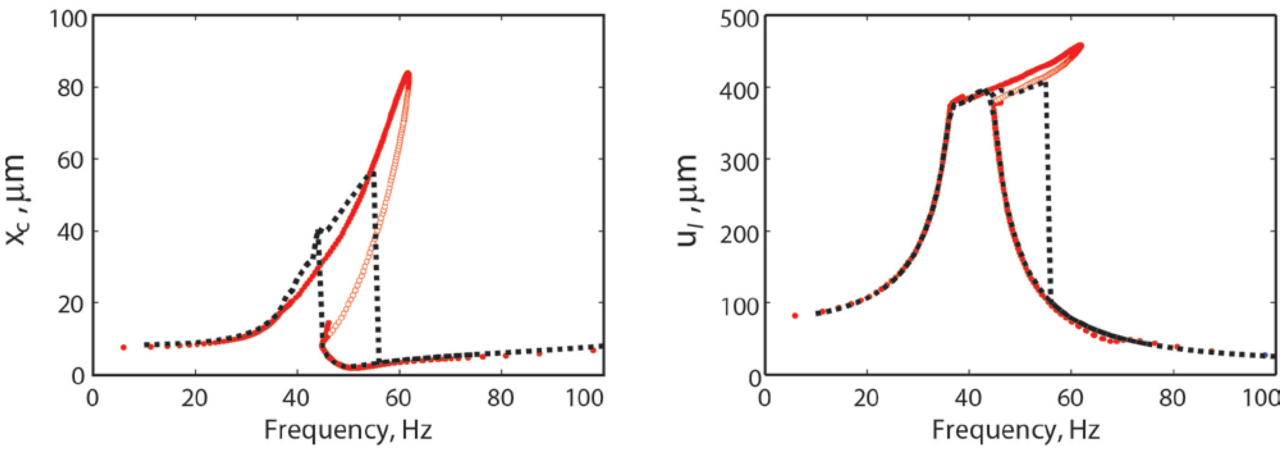

a) x_c b) u_1

Figure 6: Root-mean-square dynamic response of PG-B for various mesh frequencies calculated by the extended harmonic balance method (●) and numerical integration (--). Unstable solutions calculated by the harmonic balance method are denoted by (○).

5 Dynamic Response of Planetary Gears with Gravity

Dynamic analyses of PG-A and PG-B were performed using the extended harmonic balance approach within the speed range from 0 to 200 Hz. The response included 100 harmonics of the carrier frequency, three harmonics of the mesh frequency, and eight upper and lower side bands of the mesh frequency harmonics. These parameters were selected based on the energy distribution in the frequency spectrum of the experimental data in Figure 4.

Vibration modes of two-dimensional planetary gears include rotational modes with distinct natural frequencies, translational modes with degenerate natural frequencies of multiplicity two, and planet modes with degenerate natural frequencies of multiplicity $N-3$. Translational modes include translation but no rotation of the carrier, ring, and sun gears. The rotational modes considered have only rotation of the carrier, ring, and sun gears. The planet modes considered have only planet motions; the carrier, ring, and sun gears do not move. These vibration modes are derived from the eigenvalue problem of the equations of motion in Eq. (1) without tooth contact and bearing clearance nonlinearities. The natural frequencies of PG-A under 800 Hz are the translational modes at 165, 311, and 796 Hz and the rotational mode at 292 Hz. The natural frequencies and mode shapes of PG-B are described in Table 3.

5.1 Gravity-induced excitation

The gravity force in the rotating carrier frame is periodic about the carrier frequency and becomes an excitation source for the planetary gears. The effects of gravity and fluctuating mesh stiffness on the dynamic response of PG-B are shown in Figure 7. Within the speed range of interest, the carrier response with gravity as the excitation source is one order of magnitude higher than that with fluctuating mesh stiffness. This agrees with the observation that low-frequency external excitations have a greater contribution to the dynamic response, rather than the high-frequency internal excitation from gear meshing as measured in the experiments shown in Figure 4. In the dynamic response, with gravity as the excitation source, only the first and second translational modes are present. In the dynamic response, with fluctuating mesh stiffness as the excitation, the vibration amplitude is much lower—although more resonances are excited. This includes the first two translational modes, the fourth harmonic of the third translational mode, and the second harmonic of the rotational mode. Fluctuating mesh stiffness consists of the fundamental and higher harmonics of the mesh frequency and can thus excite gearbox vibration modes beyond the frequency range studied in Figure 7.

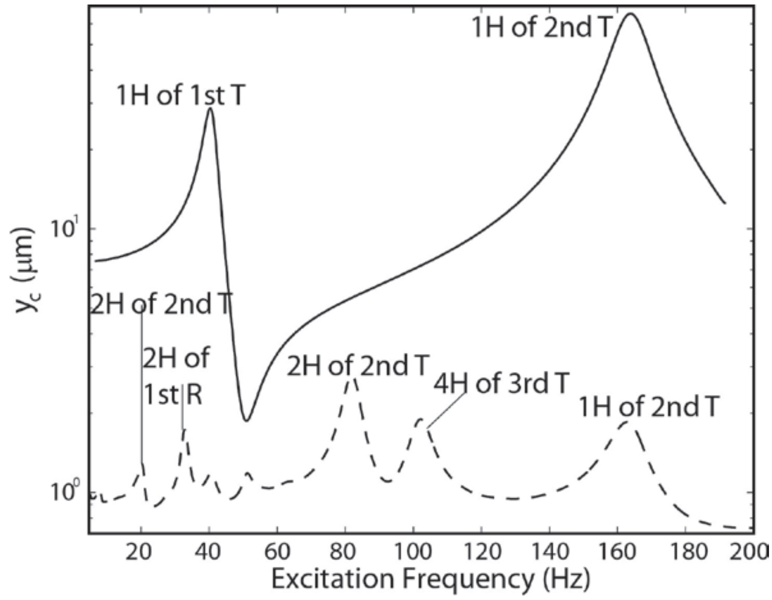

Figure 7: RMS dynamic response of PG-B carrier translational vibration with gravity (-) or mesh stiffness (--) excitations. Bearing clearance is zero, infinite backlash is used, H = harmonic mode, T = translational mode, and R = rotational mode.

5.2 Nonlinear dynamic effects

Figure 8 (a) (top) and Figure 8 (a) (bottom) show the carrier translational and rotational displacements of PG-B with different tooth backlash conditions. Backlash affects the translational mode resonance at 41 Hz as shown in Figure 8(a) (top graph) but it does not affect the carrier rotational displacement as shown in Figure 8(a) (bottom graph). With nominal backlash ($b_s = b_r = 482$ μm), the shape of the resonance peak bends toward the right. This nonlinear effect is the hardening effect caused by tooth wedging at the resonance. As the backlash decreases, the shape of the resonance bends further to the right and the resonant frequency increases from 41 to 84 Hz.

When the backlash is one-third of its nominal value, a closed loop caused by nonlinear tooth contact occurs at 70 Hz in the dynamic response of x_c. Figure 8(b) shows the tooth contact at both the drive-side and back-side of the first sun-planet mesh with one-third of the nominal backlash under the same condition as Figure 8(a). In this figure, a y-axis value of “1” indicates a full contact condition and a “0” represents an out-of-contact condition. Within the speed range of 70–85 Hz, the gear rotates significantly due to the rotational mode at 70 Hz and loses tooth contact. In the meantime, the translational mode causes the radial motion between the sun and planet 1. This radial motion exceeds the available tooth radial gap, which leads to tooth wedging. The coexistence of tooth wedging and tooth contact loss within the same speed range reflects the competition between the translational and rotational modes, resulting in the closed loop in Figure 8(a).

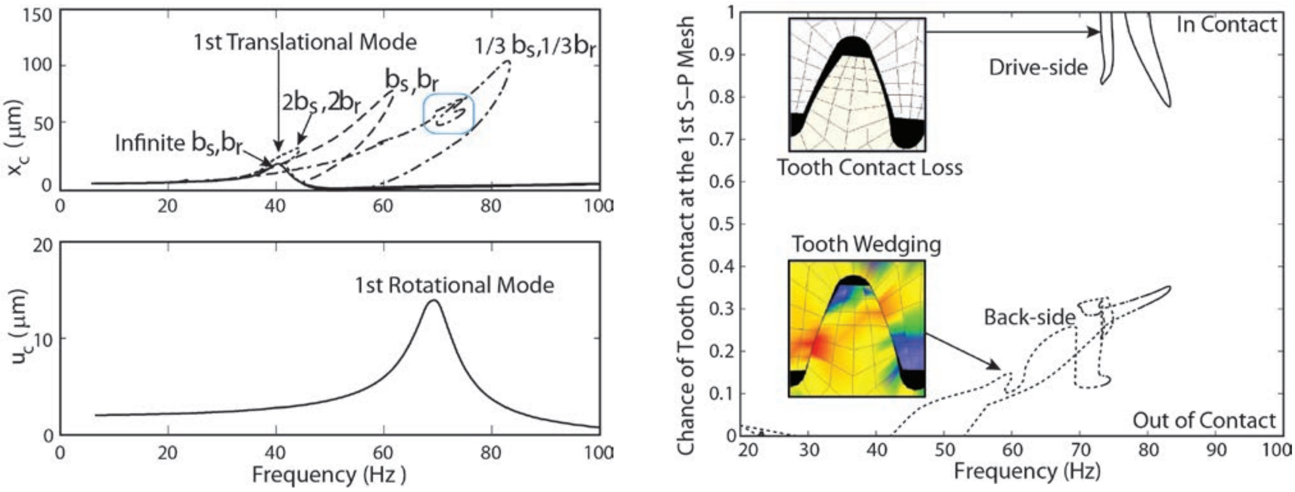

(a) (b)

Figure 8: (a) Dynamic response of the RMS of carrier translational (upper graph) and rotational (lower graph) responses of PG-B with different backlash; (b) drive-side and back-side tooth contact at the first sun-planet mesh with one-third of nominal backlash

Figure 9(a) and Figure 9(b) show the dynamic responses of x_r and ξ_1 with various values of bearing clearance for PG-A. The resonant frequency of the first translational mode reduces from 165 to 28 Hz when the bearing clearance increases from 0 to 400 μm as shown in Figure 9(a). Bearing clearance affects the resonant frequencies of the translational mode shapes of the member with the bearing clearance [4]. For large-scale wind turbine gearboxes, the resonant frequencies can be further reduced into the range of external low-speed excitations because of structural flexibilities of the drivetrain, the blades, and the supporting components [25]. The responses without clearance and with clearance of 400 μm, which is essentially infinite clearance, correspond to two limiting systems. The mode shapes of these two limiting systems are different from each other as depicted in Figure 9(a). In Figure 9(a), the ring gear displacement increases 4.6 times when clearance increases from 0 to 400 μm. In the meantime, the planet translational displacement ξ_1 decreases 25 μm when the bearing clearance increases. Clearance in the carrier bearing increases the vibration of the central members (the sun, ring, and carrier). Its effect on planet responses is much smaller. The bearing forces at the carrier support are small because they are nearly balanced by corresponding self-imposed tooth loads. Because of the absence of the nominal bearing preload, the carrier bearing clearance creates nonlinear dynamic behavior. Away from the resonance, the vibration amplitude is too low, so the bearing is not in contact. Near the resonance, the carrier bearing rolling element displacement evolves gradually from no contact to partial contact, and eventually to full contact at the resonant frequency. The carrier bearing rollers contacting the raceways at the resonant frequency induces the stiffening effects shown in Figure 9(a) and Figure 9(b). This stiffening effect reflects the increase in the overall bearing stiffness from the increased bearing contact [4].

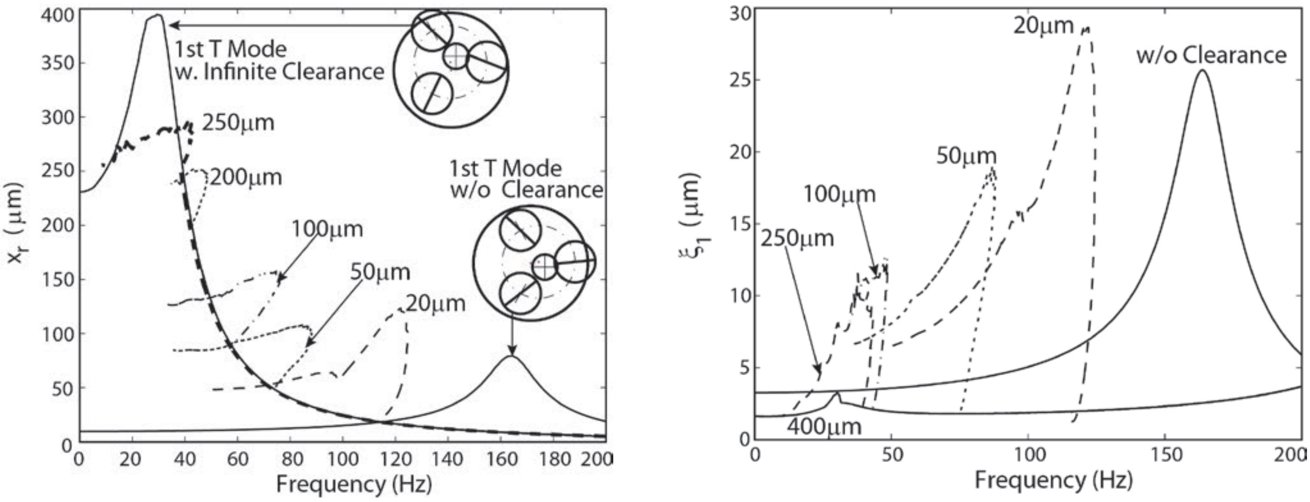

(a) x_r (b) ξ_1

Figure 9: RMS x_r and ξ_1 dynamic responses of PG-A with bearing clearance from 0 to 400 μm

5.3 Tooth wedging

Tooth wedging induced by gravity is a potential source for planet-bearing premature failures [1]. The influence of bearing clearance on tooth wedging is investigated in Figure 10. The back-side tooth load over a carrier cycle at the sun-planet mesh is compared to the average tooth load on the drive-side. The tooth loads are calculated for various values of the ratio between bearing clearance and backlash. When the bearing clearance is smaller than the backlash, there is no back-side tooth contact regardless of speed. When the bearing clearance is larger than the backlash, the back-side tooth load gradually increases with bearing clearance. When the speed is near the rpm that excites the resonant frequency, the tooth load is higher than when the excitation speed is further away from the resonant frequency. The critical clearance when tooth wedging occurs is entirely independent of speed. The critical clearance value is reached when the bearing clearance equals the backlash. Therefore, the bearing clearance should be smaller than the backlash to avoid the potential of tooth wedging in wind turbine planetary gears.

The sun support stiffness also affects tooth wedging. Figure 11 shows the back-side tooth load over a carrier cycle at various sun support stiffness values. When the bearing clearance equals or is larger than the backlash, the tooth load increases exponentially with an increase in sun support stiffness. At zero sun support stiffness, no back-side tooth contact occurs regardless of the value of bearing clearance. When bearing clearance is smaller than the backlash, the back-side tooth load is zero for small sun support stiffness values. However, when the sun support stiffness has the same order of magnitude as the ring stiffness, tooth wedging occurs even with a smaller bearing clearance than the backlash.

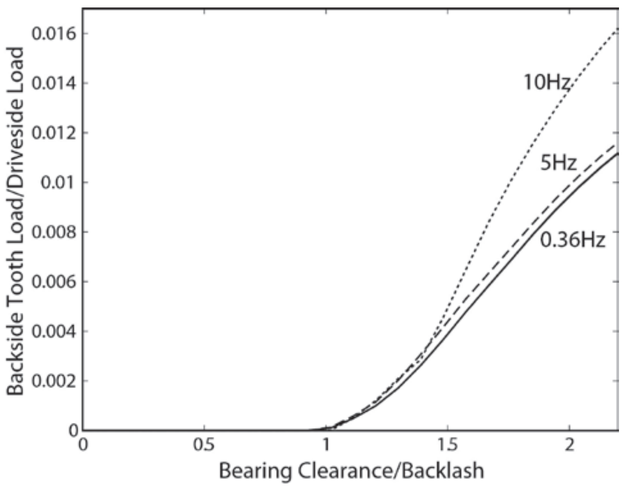

Figure 10: Average back-side tooth load at the first sun-planet mesh over a carrier cycle with various bearing clearances and speeds for PG-A

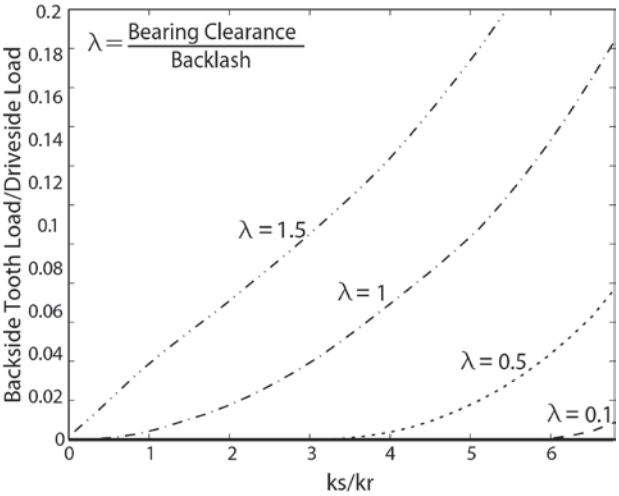

Figure 11: Average back-side tooth load at the first sun-planet mesh over a carrier cycle with various sun stiffnesses and bearing clearances for PG-A. The carrier speed is 0.5 Hz.

6 Conclusions

The extended harmonic balance method was developed to calculate the steady-state, nonlinear, dynamic response of wind turbine planetary gears having simultaneous internal and external excitation sources. Results obtained by the proposed approach compare well with the GRC experiments of PG-A at a single operational speed and the numerically integrated results of the lumped-parameter model of PG-B over a wide speed range. This approach avoids protracted time integration simulations by calculating the dynamic response in the frequency domain. The time savings of this method make it suitable for parametric studies, which could be used to tune the planetary gear dynamics during the design phase to minimize vibratory response.

Gravity in the rotating carrier frame is an important external excitation source of wind turbine planetary gears. Gravity causes tooth wedging and bearing contact at vibratory resonances, leading to stiffening effects in the dynamic response. A unique nonlinear effect induced by gravity illustrates the competition of tooth wedging and tooth contact loss in the translational and rotational modes.

Clearance in the carrier bearings reduces the resonant frequencies of the translational modes of the carrier. The shapes of these translational modes are affected by this bearing clearance.

Tooth wedging is a combined effect of bearing clearance, backlash, and sun support stiffness and can occur at a much lower speed than the planetary stage resonant frequency. Planetary gears have a risk of developing tooth wedging when the bearing clearance is larger than the backlash. When the sun support stiffness has the same order of magnitude as the gearbox mount stiffness, tooth wedging occurs even when the bearing clearance is smaller than the backlash.

7 Acknowledgements

The authors would like to thank William LaCava for providing the experimental data used in this work. The Gearbox Reliability Collaborative (GRC) project at the National Renewable Energy Laboratory (NREL), Colorado, USA, is funded by the Wind and Water Power Program of the U.S. Department of Energy.

References

[1] Y. Guo and R. G. Parker, "Dynamic modeling and analysis of a spur planetary gear involving tooth wedging and bearing clearance nonlinearity," *European Journal of Mechanics A/Solids,* vol. 29, pp. 1022-1033, 2010.

[2] A. Kahraman and R. Singh, "Nonlinear dynamics of a geared rotor-bearing system with multiple clearances," *Journal of Sound and Vibration,* vol. 144, pp. 469-506, 1991.

[3] N. E. Gurkan and H. Ozguven, "Interactions between backlash and bearing clearance nonlinearity in geared flexible rotors," in *ASME International Design Engineering Technical Conferences and Computers and Information in Engineering Conference*, 2007.

[4] Y. Guo and R. G. Parker, "Dynamics of planetary gears with bearing clearance," *ASME Jounal of Computational Nonlinear Dynamics,* vol. 7, no. 3, p. 031008, 2012.

[5] S. Vijayakar, "A combined surface integral and finite-element solution for a 3-dimensional contact problem," *International Journal for Numerical Methods in Engineering,* vol. 31(3), p. 525–545, 1991.

[6] V. K. Ambarisha and R. G. Parker, "Nonlinear Planetary Gear Dynamics using Analytical and Finite Element Models," *Journal of Sound and Vibration,* vol. 302, pp. 577-595, 2007.

[7] P. Velex and L. Flamand, "Dynamic response of planetary trains to mesh parametric excitations," *Journal of Mechanical Design,* vol. 118, no. 1, pp. 7-14, 1996.

[8] J. Thomsen, Vibration and Stability: Advanced Theory, Analysis, and Tools., 2nd, Ed., Springer, 2003.

[9] F. Zhu and R. Parker, "Non-linear dynamics of a one-way clutch in belt-pulley systems," *Journal of Sound and Vibration,* vol. 279, pp. 285-308, 2005.

[10] G. W. Blankenship and A. Kahraman, "Steady state forced response of a mechanical oscillator with combined parametric excitation and clearance type non-linearity," *Journal of Sound and Vibration,* vol. 185, no. 5, pp. 743-765, 1995.

[11] A. Kahraman and G. W. Blankenship, "Experiments on nonlinear dynamic behavior of an oscillator with clearance and periodically time-varying parameters," *Journal of Applied Mechanics,* vol. 64, pp. 217-226, 1997.

[12] A. Al-shyyab and A. Kahraman, "Non-linear dynamic analysis of a multi-mesh gear train using multi-term harmonic balance method: period-one motions," *Journal of Sound and Vibration,* vol. 284, no. 1-2, pp. 151-172, 2005.

[13] A. Al-shyyab and A. Kahraman, "Non-linear dynamic analysis of a multi-mesh gear train using multi-term harmonic balance method: subharmonic motions," *Journal of Sound and Vibration,* vol. 279, no. 1-2, pp. 417-451, 2005.

[14] C.-J. Bahk and R. Parker, "Analytical solution for the nonlinear dynamics of planetary gears," *ASME Journal of Computational and Nonlinear Dynamics,* vol. 6, no. 2, p. 021007, 2011.

[15] A. Nayfeh and B. Balachandran, Applied Nonlinear Dynamics, John Wiley and Sons, 1995.

[16] A. Raghothama and S. Narayanan, "Bifurcation and chaos in geared rotor bearing system by incremental harmonic balance method," *Journal of Sound and Vibration,* vol. 226, no. 3, pp. 469-492, 1999.

[17] R. Seydel, Practical bifurcation and stability analysis: from equilibrium to chaos, 2nd, Ed., Springer, 1994.

[18] Y. Guo, J. Keller and R. G. Parker, "Dynamic Analysis of Heavy Duty Planetary Gears with Gravity Effects," *Wind Energy,* vol. In preparation, 2012.

[19] K. Turner and H. F. Walker, "Efficient high accuracy solutions with gmres (m)," *Journal on Scientific and Statistic Computing,* vol. 13, no. 3, p. 815825, 1992.

[20] L. Grippo, F. Lampariello and S. Lucidi, "A Nonmonotone Line Search Technique for Newton's Method," *SIAM Journal on Numerical Analysis,* vol. 23, no. 4, pp. 707-716, 1986.

[21] H. Link, W. LaCava, J. V. Dam, B. McNiff, S. Sheng, R. Wallen, M. McDade, S. Lambert, S. Butterfield and F. Oyague, "Gearbox reliability collaborative project report: findings from phase 1 and phase 2 testing," NREL technical report: NREL/TP-5000-51885, 2011.

[22] F. Rasmussen, K. Thomsen and T. Larsen, "The Gearbox Problem Revisited. Fact Sheet AED-RB-17 (EN).," Risoe National Laboratory, Denmark., 2004.

[23] Y. Guo, J. Keller and W. LaCava, "Combined Effects of Input Torque, Non-Torque Load, Gravity, and Bearing Clearance on Planetary Gear Load Share in Wind Turbine Drivetrains," in *AGMA fall technical meeting*, 2012.

[24] F. Oyague, D. Gorman and S. Sheng, "NREL Gearbox Reliability Collaborative Experimental Data Overview and Analysis," in *Windpower Conference and Exhibition*, Texas, 2010.

[25] J. Helsen, F. Vanhollebeke, F. D. Coninck, D. Vandepitte and W. Desmet, "Insights in wind turbine drive train dynamics gathered by validating advanced models on a newly developed 13.2 MW dynamically controlled test-rig," *Mechatronics,* vol. doi:10.1016/j.mechatronics.2010.11.005.

Appendix: Gearbox Parameters

	Sun	Ring	Carrier	Planet
Mass (kg)	181.6	2,633	759.9	104
Moment of Inertia (kg-m^2)	3.2	144.2	59.1	3.2
Number of Teeth	21	39	-	99
Pitch Diameter (mm)	215.6	400.4	-	1,016.4
Root Diameter (mm)	186.0	372.9	-	-
Average Mesh Stiffness (N/m)	k_{sp} = 16.9 x 10^9, k_{rp} = 19.2 x 10^9			
Bearing Stiffness (N/m)	100	102 x 10^6	5 x 10^9	6.8 x 10^9
Carrier Bearing Stiffness (N/m)	3.2 x 10^9			
Carrier Bearing Clearance (mm)	0.275			
Torsional Support Stiffness (N-m)	45.8 x 10^6	57.4 x 10^6	0	0

Table 1: System parameters for the 750-kW Gearbox Reliability Collaborative (GRC) planetary gearbox (PG-A). The ring mass includes the gearbox housing and parallel stages.

	Sun	Ring	Carrier	Planet
Mass (kg)	51	4,000	1,330	114
Moment of Inertia (kg)	61.1	2,484	314.7	51.9
Number of Teeth	16	68	-	26
Root Diameter (mm)	202	980	-	329
Pitch Diameter (mm)	224	952	-	364
Average Mesh Stiffness (N/m)	k_{sp} = 3.95 x 10^9, k_{rp} = 5.29 x 10^9			
Bearing Stiffness (N/m)	100	126 x 10^6	4 x 10^9	5.3 x 10^9
Carrier Bearing Stiffness (N/m)	3.6 x 10^9			
Carrier Bearing Clearance (mm)	1			
Torsional Support Stiffness (N-m)	3 x 10^6	24.4 x 10^6	0	0

Table 2: System parameters for the 550-kW planetary gearbox (PG-B). The ring mass includes the gearbox housing and parallel stages.

Natural Frequency Lumped-parameter (Hz)	Natural Frequency Finite Element (Hz)	Deviation	Mode Type	Modal Damping
40.75	40.94	0.35%	Translational	5.48%
69.49	69.1	0.56%	Rotational	5.26%
157.53	163.7	3.77%	Translational	7.43%
301.46	312.1	3.41%	Rotational	5.19%

Table 3: Natural frequencies of PG-B.